Asymmetries in mixed beauty decays

de Vries, J.A.

2018

document version
Publisher's PDF, also known as Version of record

5 *CP* violation in mixing of B_s^0 mesons

This chapter details the analysis of *CP* violation in mixing of B_s^0 mesons, which is quantified by the parameter $a_{\rm sl}^s$. This measurement is published in Ref. [108]. The definition of this parameter is outlined in Sec. 1.2.8, and the measurement employs the techniques from Sec. 3 to determine the detection asymmetries.

5.1 Method

The B_s^0 decays are reconstructed in the decay channel

$$B_s^0 \to D_s^- \mu^+ \nu_\mu X \quad \text{with} \quad D_s^- \to K^- K^+ \pi^-$$

and their charge-conjugate modes, where the X represents any number of additional particles — besides the neutrino — that are not explicitly reconstructed in the decay. The decay topology is illustrated by Fig. 5.1, and is similar to the $a_{\rm sl}^d$ analysis as the only difference is that the $D^-(\to K^+\pi^-\pi^-)$ is replaced by $D_s^-(\to K^+K^-\pi^-)$. Also, here in the $a_{\rm sl}^s$ analysis the non-reconstruction of the additional particles results in a broad invariant mass peak for the B_s^0 candidates.

In contrast to the $a_{\rm sl}^d$ analysis, due to the fast mixing frequency Δm_s the time-dependent effect washes out and it is sufficient to measure the time-integrated asymmetries (see Sec. 1.2.8). The measured asymmetry in the charge-conjugated signal candidates is

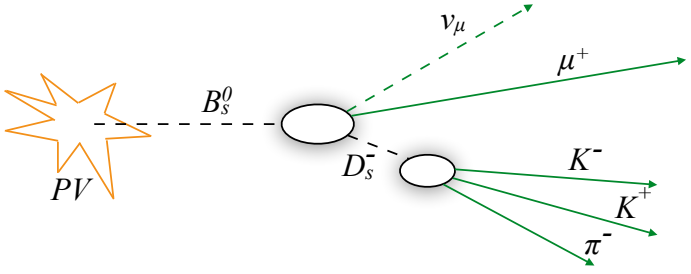

Figure 5.1: Decay topology of the $a_{\rm sl}^s$ signal decay mode.

corrected for the effect of backgrounds and for the detection asymmetry in order to obtain $a^s_{\rm sl}$, as in Eq. 1.2.43. It is rewritten here for convenience,

$$A_{\rm meas} = \frac{N(D_s^-\mu^+) - N(D_s^+\mu^-)}{N(D_s^-\mu^+) + N(D_s^+\mu^-)},$$
$$a^s_{\rm sl} = \frac{2}{1-f_{\rm bkg}}(A_{\rm meas} - A_{\rm det} - f_{\rm bkg}A_{\rm bkg}) \tag{5.1.1}$$

Here, $f_{\rm bkg}$ is the fraction of peaking backgrounds that dilute the measurement of $a^s_{\rm sl}$, and $A_{\rm bkg}$ is the total (production + physics) asymmetry of these backgrounds that can bias the value of $a^s_{\rm sl}$. The selection of data is described in Sec. 5.2, where non-peaking backgrounds are reduced. The contribution of peaking backgrounds, originating from other b-hadron decays, is determined in Sec. 5.3, the relevant detection asymmetries are discussed in Sec. 5.4 and the results are shown in Sec. 5.5.

5.2 Selection

Similar to the $a^d_{\rm sl}$ analysis, this analysis makes use of the full LHCb dataset obtained during run 1 of the LHC. This equals integrated luminosities of $1.0\,{\rm fb}^{-1}$ at a centre-of-mass energy of 7 TeV obtained in 2011, and $2.0\,{\rm fb}^{-1}$ at 8 TeV obtained in 2012.

The event is required to be triggered by the muon from the semileptonic B_s^0 decay on the hardware level. At the first software stage, the event is required to be triggered by the muon only (`Hlt1TrackMuon`), or any of the tracks using a more stringent trigger (`Hlt1TrackAllL0`). At the second software stage, the decay topology of the reconstructed B_s^0 candidate is required to be consistent with a b-hadron decay. The precise requirements made in the trigger are described in Sec. 2.4.

In the offline selection, standard quality requirements on the reconstructed tracks and vertices are made to form B_s^0 signal candidates. Similar as in the $a^d_{\rm sl}$ analysis, the final-state tracks are required to not point back to the primary vertex, in order to reduce backgrounds from promptly produced particles. An additional selection is made to reduce various sources of backgrounds, some of which are similar to those in the $a^d_{\rm sl}$ analysis. The decay $D_s^- \to K^+K^-\pi^-$ can occur through resonant states, which are treated separately in this analysis.[1] The dominant resonances are the $\phi(1020) \to K^+K^-$ and the $K^*(892) \to K^+\pi^-$ decays, which are visible in the invariant mass of two-daughter combinations, as shown in Fig. 5.2. Three regions in this so-called Dalitz plane of the $D_s^- \to K^+K^-\pi^-$ decay are selected:

- $\phi\pi$: Invariant mass of the K^+K^- pair within $\pm 20\,{\rm MeV}/c^2$ of the narrow ϕ mass of $1020\,{\rm MeV}/c^2$,
- K^*K : Invariant mass of the $K^+\pi^-$ pair within $\pm 90\,{\rm MeV}/c^2$ of the broader K^* mass of $892\,{\rm MeV}/c^2$,

[1] In the $a^d_{\rm sl}$ analysis, there is a large overlap between resonances in the $D^- \to K^+\pi^-\pi^-$ decay, and they are not separated.

- NR : non-resonant, i.e. all remaining phase space ,

which have different amounts of background, as well as different kinematic distributions for the daughter $K^+K^-\pi^-$ particles. Therefore, the selection is optimized separately for each of the three regions. The largest signal-to-background ratio is obtained in the $\phi\pi$ region, followed by the K^*K region. Since the sample contains less background, the $\phi\pi$ region has looser PID requirements compared to the selection used for the K^*K and NR regions.

The value for $a^s_{\rm sl}$ will be determined separately for each magnet polarity, data-taking year and Dalitz region, and checked for consistency between these twelve values. Then, the raw asymmetry and various detection asymmetries will be averaged, and combined to obtain the overall value for $a^d_{\rm sl}$.

5.2.1 Removal of identifiable backgrounds

Contributions from backgrounds under the D_s^- invariant mass peak are further reduced with specific selection criteria. Most of these backgrounds originate from misidentification of the kaon that has the same sign as the D_s^- candidate. These identifiable background contributions can be visualized by using the momentum asymmetry of this kaon (here K^-) with respect to the other two particles,

$$\beta = \frac{p_{K^+} + p_{\pi^-} - p_{K^-}}{p_{K^+} + p_{\pi^-} + p_{K^-}}. \tag{5.2.1}$$

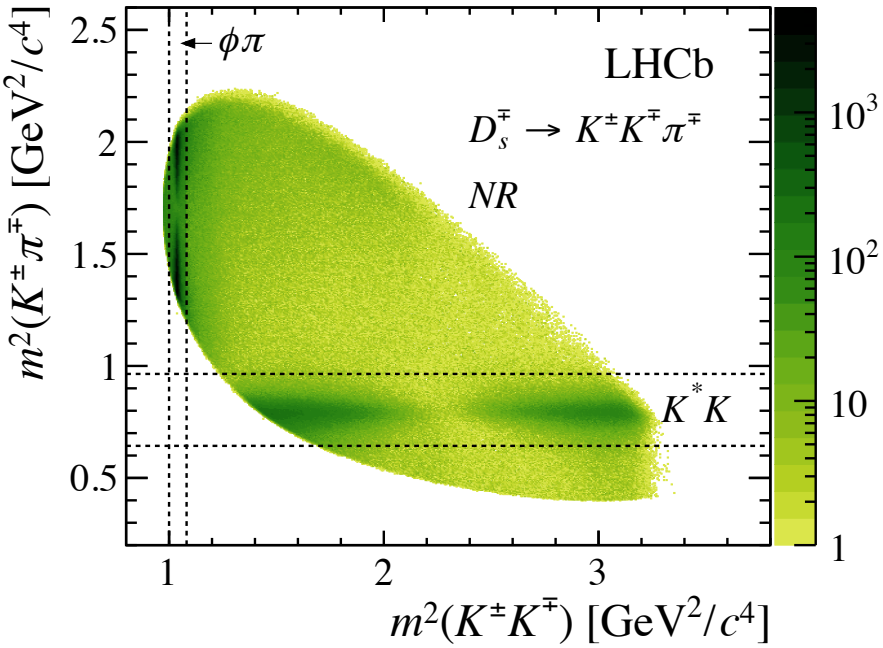

Figure 5.2: Dalitz plot of the $D_s^- \to K^-K^+\pi^-$ decay for selected $D_s^-\mu^+$ candidates, with the three selection regions indicated. To suppress combinatorial background, a narrow invariant mass window, between 1950 and 1990 MeV/c^2, is required for the D_s^- candidates in this plot.

When looking at the invariant mass $M_{K^-K^+\pi^-}$ versus β for all D_s^- candidates, the contributions from misidentified K^- backgrounds have a well-defined dependence on β, while correctly identified candidates have no dependence on β. The D_s^- candidate invariant mass is different for either the correct hypothesis m_{K^-} or an alternative wrong hypothesis m_{alt}. This difference can be parametrized as

$$M^2_{K^-K^+\pi^-} - M^2_{\text{alt}} \approx (m^2_{K^-} - m^2_{\text{alt}})\frac{2}{1-\beta}, \tag{5.2.2}$$

which follows from relativistic mechanics, and where an approximation is made for $m/p \ll 1$ for all final-state particles. M^2_{alt} is the D_s^- candidate mass under a mass hypothesis m_{alt} of the K^- candidate.

The left column of Fig. 5.3 shows these plots for the three different Dalitz regions. The signal is seen as a band around 1970 MeV/c^2, and the correctly identified but Cabibbo-suppressed $B_s^0 \to D^-(K^-K^+\pi^-)\mu^+\nu_\mu$ decays are visible in these plots around 1870 MeV/c^2.

The reduction of the non-peaking backgrounds is optimized using simulated events, combined with studies on data using the sidebands around the D_s^- peak. In general, misidentified backgrounds are reduced by requiring an additional neural-net-based PID cut on the same-sign kaon for all three Dalitz regions. Specific backgrounds are reduced further by applying a veto under certain mass hypotheses, as is done in the a^d_{sl} analysis in Sec. 4.2. A list of veto criteria that are applied is summarized in Table 5.1.

In all modes there is a clear contribution from misidentified $\overline{\Lambda}_b^0 \to \Lambda_c^+(p^-K^+\pi^-)\mu^+\nu_\mu$ decays. These decays are especially abundant in the K^*K and NR samples. They are reduced by applying a tight PID cut on the kaon with the same sign as the D_s^-, when the invariant mass of the D_s^- candidate under the proton hypothesis for the kaon, $M(K^-_{p^-}K^+\pi^-)$, is within 27 MeV/c^2 of the $\overline{\Lambda}_c^-$ mass. The subscript p^- denotes which particle was misidentified.

In the K^*K and NR samples the contribution from misidentified $B^0 \to D^-(\pi^-K^+\pi^-)\mu^+\nu_\mu$ decays is removed by applying a similar a cut if the invariant mass

Table 5.1: Summary of the applied vetoes used to reduce specific non-peaking backgrounds under the D_s^+ mass peak, in order of appearance in the text. The subscript of a particle denotes the (misidentified) mass hypothesis that is applied.

Veto	Veto if	Applied to
$\Lambda_c^+ \to p_K K\pi$	K^+ $\texttt{DLL}_{p-K} > 0.0$ and $2261 < m(K^+_p K^-\pi^+) < 2315$ MeV/c^2	$\phi\pi$
$\Lambda_c^+ \to p_K K\pi$	K^+ $\texttt{DLL}_{p-K} > -15.0$ and $2261 < m(K^+_p K^-\pi^+) < 2315$ MeV/c^2	K^*K, NR
$D^+ \to \pi_K K\pi$	K^+ $\texttt{DLL}_{K-\pi} < 30.0$ and $\lvert m(K^+_\pi K^-\pi^+) - 1870\rvert < 20$ MeV/c^2	K^*K, NR
$D^*(\to D^0(\to K\pi_K\pi\pi))$	K^+ $\texttt{DLL}_{K-\pi} < 7.0$ and $m(K^+{}_\pi K^-) < 800$ MeV/c^2	K^*K, NR
$D^*(\to D^0\pi_K)$	$m(K^+_\pi K^-\pi^+) - m(K^-\pi^+) < 175$ MeV/c^2	K^*K, NR
$D^*(\to D^0\pi_K)$	$m(K^+K^-_\pi\pi^+) - m(K^+\pi^+) < 175$ MeV/c^2	K^*K, NR
$D \to K^*(892)^0(\to K\pi_K)\pi$	K^+ $\texttt{DLL}_{K-\pi} < 8.0$ and $\lvert m(K^+_\pi K^-) - 892\rvert < 25$ MeV/c^2	K^*K, NR
$J/\psi \to \mu_\pi\mu$	π^+ in muon stations, $3042 < m(\pi^+_\mu\mu^-) < 3147$ MeV/c^2	$\phi\pi$, K^*K, NR
$J/\psi \to \mu_K\mu$	K^+ in muon stations, $3042 < m(K^+_\mu\mu^-) < 3147$ MeV/c^2	K^*K, NR
$D^{*+} \to D^0(K^+K^-)\pi^+$	$135 < m(K^+K^-\pi^+) - m(K^+K^-) < 152$ MeV/c^2	NR

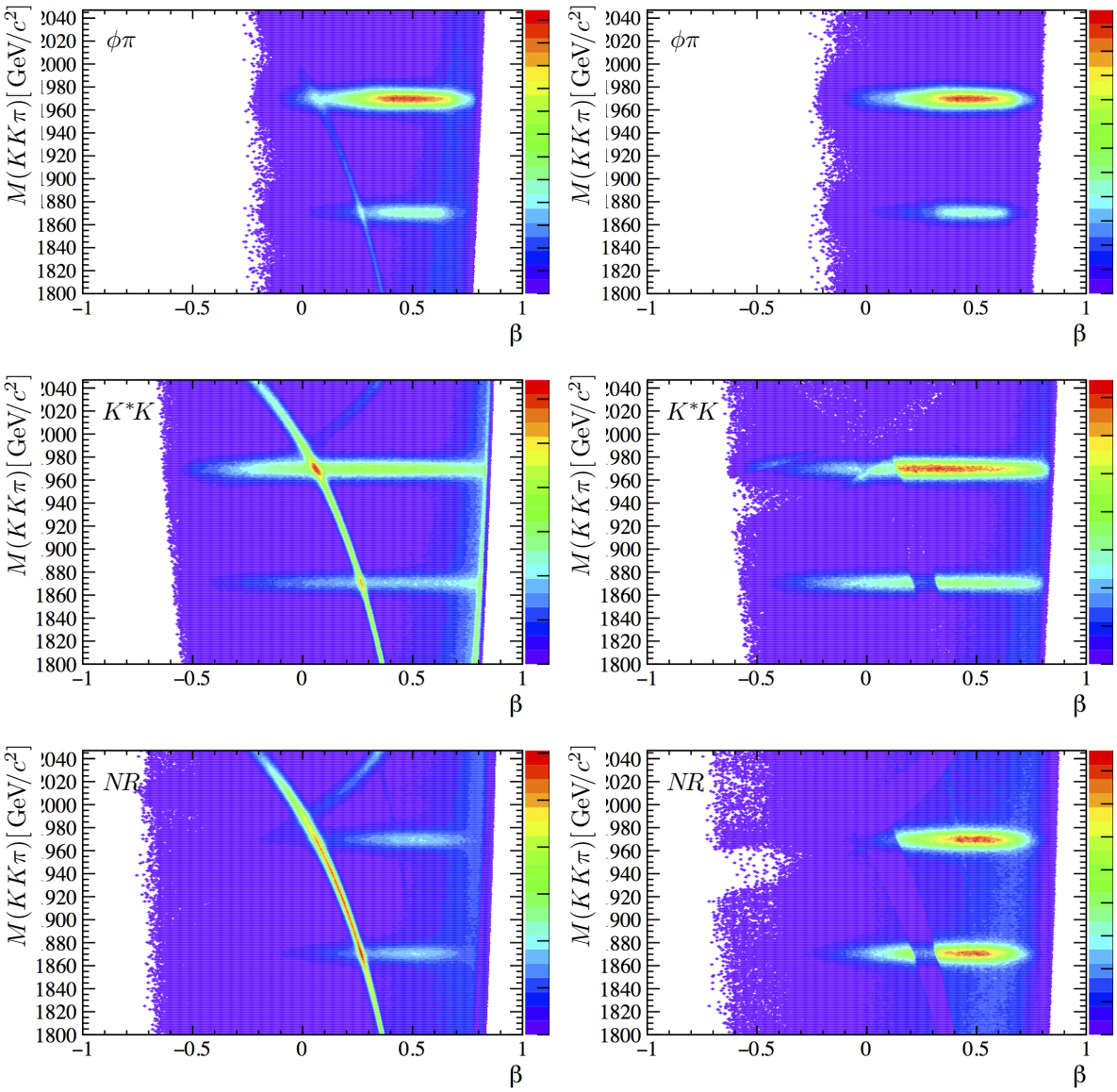

Figure 5.3: $M_{K^+K^-\pi^+}$ versus the momentum asymmetry of the same-sign kaon, β (Eq. 5.2.1), for (top) the $\phi\pi$ region, (middle) the K^*K region, and (bottom) NR region, (left) before and (right) after the vetoes in Table 5.1 and the neural-net-based PID criterium. The horizontal bands correspond to the correctly identified D_s^- and (Cabibbo-suppressed) D^- decays, while the downward-curving and upward-curving bands in the plots correspond to the misidentified $\overline{\Lambda}_c^-$ and D^- backgrounds, respectively. The contribution from $D^{*-} \to D^0(\to K^+\pi^-\pi^+\pi^-)\pi^-$ decays is seen as a faint band on the right side of the plots.

$M(\pi^-{}_{K^-}K^+\pi^-)$ is within $20\,\mathrm{MeV}/c^2$ of the D^- mass. This contribution is not visible in the $\phi\pi$ sample. The contribution of these $\overline{\Lambda}_c^-$ and D^- backgrounds after these vetoes is found to be negligible for the K^*K and NR regions, and of subpercent level in the $\phi\pi$ region.

The (faint) band on the right of the spectra of Fig. 5.3 is due to the contribution of partially reconstructed backgrounds, and mainly consists of $B \to D^{*-}(\to D^0(\to K^+\pi^-\pi^+\pi^-)\pi^-{}_s)\mu^+\nu_\mu$ decays where a pion is misidentified as a kaon. About half of this background is removed by the general neural-net-based PID criterium. In the K^*K and NR regions, these candidates are reduced further by removing events where the invariant mass of the K^-K^+ pair, under the $K^-\pi^+$ mass hypothesis, falls below $800\,\mathrm{MeV}/c^2$ and the PID of the K^+ is not incompatible with that of a pion. Furthermore, events where the misidentified kaon is the soft π^- that comes directly from a D^{*-} decay are removed by applying a cut on the invariant mass difference $M(K^\pm{}_{\pi^\pm}K^\mp\pi^-) - M(K^\mp\pi^-) < 175\,\mathrm{MeV}/c^2$ for both kaons.

Further backgrounds originate from $K^{*0}(\to K^-\pi^+)\pi^-$ final states where the π^+ is misidentified as a K^+. These are removed if the K^-K^+ combination under the $K^-\pi^+$ mass hypothesis is within $25\,\mathrm{MeV}/c^2$ of the $K^{*0}(892)$ mass, and the PID of the K^+ is compatible with that of a pion.

Another background originates from $B \to J/\psi\, X$ decays, where one muon is associated with the semileptonic decay, and the other muon is misidentified as a pion or kaon and forms a D_s^- candidate with particles from the rest of the decay. They are removed by a veto on the invariant mass of μ^+K^- or $\mu^+\pi^-$ pair (under the $\mu^+\mu^-$ mass hypothesis) if it is within $50\,\mathrm{MeV}/c^2$ of the known J/ψ mass, and the pion/kaon has hits in the muon stations.

Finally, in the NR region a contribution containing correctly identified $D^{*-} \to D^0(\to K^-K^+)\pi^-$ decays are found. These are removed by a veto on the mass difference $M(K^-K^+\pi^-) - M(K^-K^+)$ to not be within $7\,\mathrm{MeV}/c^2$ of the $D^{*-} - D^0$ mass. The momentum asymmetry plots after the vetoes are shown in the right column of Fig. 5.3. The dark bands indicate the successful removal of $\overline{\Lambda}_c^-$ and D^- backgrounds due to these vetoes.

The fits with full selection applied, but without the vetoes, are shown in Fig. 5.4. Before the vetoes, the background in the invariant mass is not quite flat, mostly due to the misidentified D^- background. Therefore, an additional component is added in these fits, to the right of the D_s^- signal peak, shown in grey. The result of the fits after applying the vetoes from Table 5.1 are shown in Fig. 5.7. Moreover, studies done on simulated events show that the shape of the background under the D_s^- mass peak can be described by a first-order Chebychev function. Hence, possible remaining backgrounds are absorbed in the combinatorial background component of the fit model. The size of this component is determined independently for $B_s^0 \to D_s^-\mu^+\nu_\mu$ and $\overline{B}_s^0 \to D_s^+\mu^-\overline{\nu}_\mu$ candidates, to allow for potential charge asymmetric effects in the background.

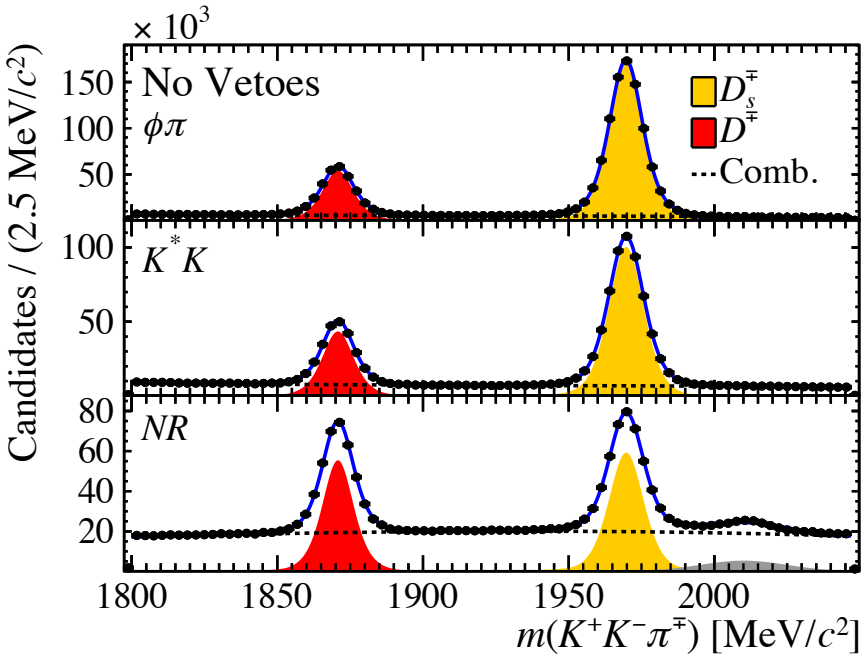

Figure 5.4: Fits to the $D_s^{\mp}$ invariant mass, for the sum of $B_s^0 \to D_s^- \mu^+ \nu_\mu$ and $\overline{B}_s^0 \to D_s^+ \mu^- \overline{\nu}_\mu$ candidates, separately for the three Dalitz regions, after full selection but without applying the vetoes from Table 5.1. Both magnet polarities and data-taking years are added. The $D_s^{\mp}$ signal yield is indicated in yellow, while the $D^{\mp}$ yield is indicated in red. In order to take into account the contribution from backgrounds, the Chebychev function is changed from first-order to second-order, and an additional Gaussian function is added to account for D^+ decays in grey.

5

5.2.2 Peaking backgrounds

Similar to the a_{sl}^d analysis, a significant fraction of background originates from real D_s^- mesons, and are included in the fitted signal yields. The various contributing decays are studied in detail in Sec. 5.3.

The contribution of promptly produced D_s^- mesons is estimated using a fit to the logarithm of the IP distribution in the data, where the shape of the distribution from simulated prompt D_s^- decays is used. This is shown in Fig. 5.5. The contribution of prompt D_s^- candidates is reduced to about 0.1% by placing a cut at $\log(\text{IP}/\,\text{mm}) > -3$, and can safely be ignored.

Contributions from other b-hadron decays have at least one additional track in the final state, and thus a lower reconstructed B_s^0 mass. Even more discriminating is the corrected B_s^0 mass, as was defined in Eq. 4.3.3. Reconstructed and corrected mass distributions for simulated signal decays, as well as various other simulated b-hadron decays, are shown in Fig. 5.6. A cut is placed at $M_{\text{corr}} > 4200\,\text{MeV}/c^2$ to reduce these backgrounds without losing too much signal candidates. Finally, a cut on the minimum (transverse) momenta of the final-state particles is made in order to match the cuts made on the calibration samples, which are used to determine the detection asymmetries. The most important

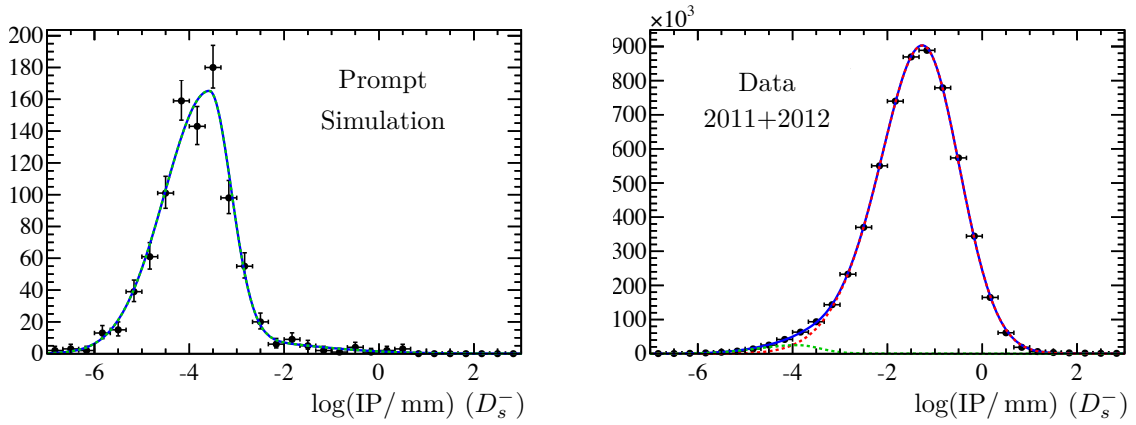

Figure 5.5: Logarithm of the impact parameter of the D_s^- candidates in (left) simulation of prompt $D_s^+ \to K^-K^+\pi^+$ decays, and (right) in data. The fit shapes are overlaid. In data the shapes are fixed from the fit to the simulated samples: in green the prompt charm contribution (as obtained from the left plot), and in red the signal contribution.

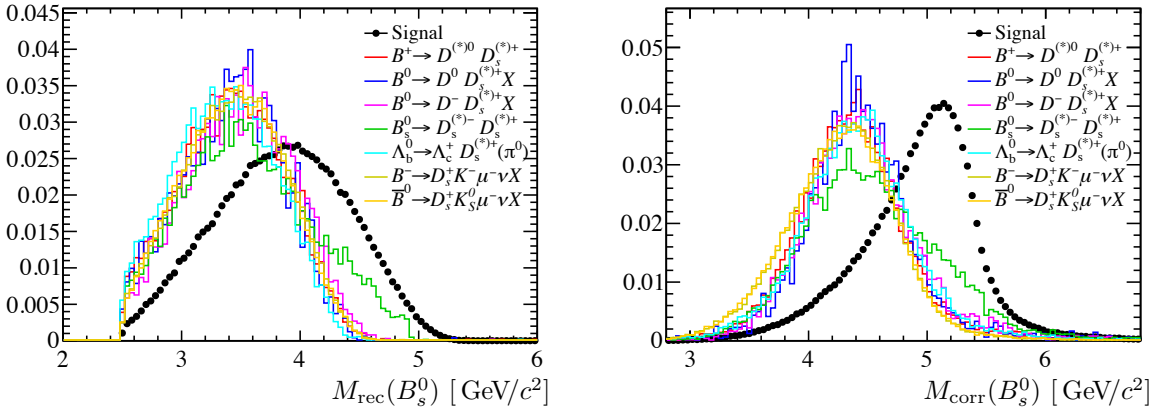

Figure 5.6: (left) Reconstructed and (right) corrected mass of the simulated B_s^0 signal candidates, and various backgrounds in simulation.

cuts made in the selection are summarized in Table 5.2. The total selection efficiency of these backgrounds will be described in Sec. 5.3.

5.2.3 Fit strategy and measured asymmetry

The measured asymmetry is obtained by performing a fit to the D_s^- invariant mass, separately for each Dalitz region. A wide D_s^- mass window of $[1800, 2047]\,\text{MeV}/c^2$ is used (see Fig. 5.4) in order to constrain the combinatorial background component. This window includes a peak from Cabibbo-suppressed but correctly identified D^- decays around $1870\,\text{MeV}/c^2$. The signal D_s^- peak, as well as the D^- peak are modelled with a double-sided Hypatia function [109], which consists of a Gaussian core with asymmetric

Table 5.2: Most important selection criteria applied to the a^s_{sl} signal sample. The definitions of the PID variables `DLL` and `ProbNN` are explained in Sec. 2.3.4. The "same-sign" kaon is the kaon with the same charge as the D_s^-. If the "applied to" field is empty, the cut is applied to all three Dalitz regions.

	Variable	**Cut**	**Applied to**
Offline cuts	D_s^- $\log(\text{IP}/\,\text{mm})$	> -3.0	
	B_s^0 M_{corr}	$> 4200\,\text{MeV}/c^2$	
	B_s^0 M_{rec}	$< 5200\,\text{MeV}/c^2$	
	D_s^- M_{rec}	$\in [1800, 2047]\,\text{MeV}/c^2$	
Calibration cuts	muon p_{T}	$> 1.2\,\text{GeV}/c$	
	muon p	$> 6.0\,\text{GeV}/c$	
	kaons p_{T}	$> 300\,\text{MeV}/c$	
	kaons p	$> 2.0\,\text{GeV}/c$	
	pion p_{T}	$> 400\,\text{MeV}/c$	
	pion p	$> 5.0\,\text{GeV}/c$	
PID cuts	muon $\texttt{DLL}_{\mu-\pi}$	> 0	
	kaons $\texttt{DLL}_{K-\pi}$	> -5.0	$\phi\pi$
	kaons $\texttt{DLL}_{K-\pi}$	> 4.0	K^*K, NR
	same-sign kaon `ProbNNk`	> 0.1	$\phi\pi$
	same-sign kaon `ProbNNk`	> 0.15	K^*K, NR
	pion $\texttt{DLL}_{K-\pi}$	< 10.0	K^*K, NR
Vetoes	See Table 5.1		

tails. These tails are an effective parametrisation of the varying mass resolution on a per-event basis. The parameters that describe the tails are fixed from a fit to the data of both magnet polarities and data-taking years combined. The background is modelled with a first-order Chebychev polynomial.

A simultaneous fit to the D_s^- and D_s^+ invariant mass is performed, and the asymmetry between the D_s^- and D_s^+ yields is a parameter in the fit. Separate parameters are used for a possible asymmetry in the D^- and D^+ yields and in the combinatorial background. The mean of the D_s^- and D_s^+ peaks, as well as the mean of the D^- and D^+ peaks are allowed to vary independently to allow for a shift in invariant mass due to misalignment effects.

The fits to the invariant mass, split up by Dalitz region, are shown in Fig. 5.7. The fits to the data spit up by magnet polarity and data-taking year are shown in Appendix C. The total $D_s^\pm$ yields after the full selection are shown in Table 5.3. The $\phi\pi$ region contains the most candidates, while the K^*K and NR regions contribute respectively a half and a third of that amount.

The measured asymmetries are shown in Table 5.3. The combination is made by adding the three Dalitz regions with weights. The weights for each Dalitz region are obtained from the combined statistical error on the measured asymmetry and detection asymmetries, and are 0.61 for the $\phi\pi$ region, 0.25 for the K^*K region and 0.14 for the NR region. The

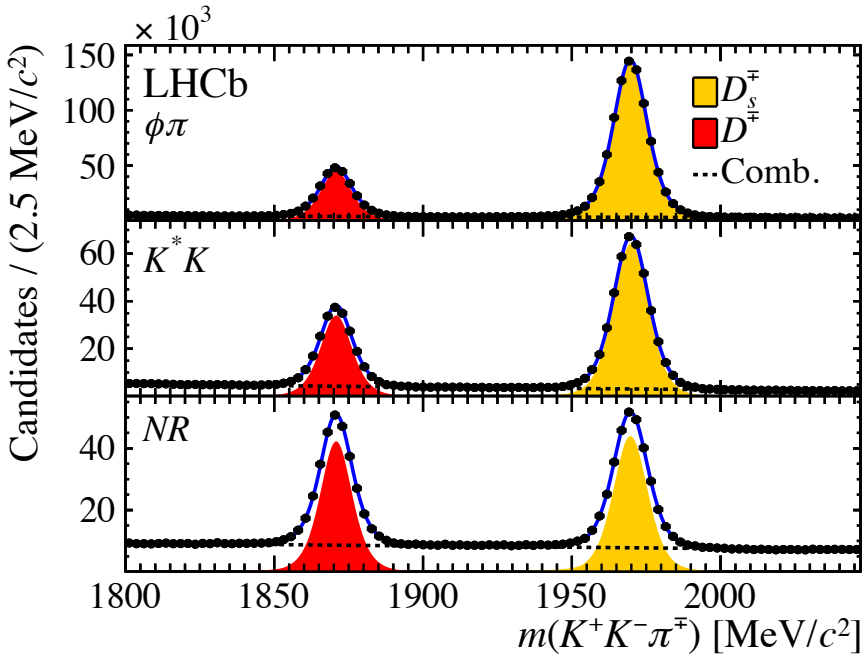

Figure 5.7: Fits to the $D_s^{\mp}$ invariant mass, for the sum of $B_s^0 \to D_s^- \mu^+ \nu_\mu$ and $\overline{B}_s^0 \to D_s^+ \mu^- \overline{\nu}_\mu$ candidates, separately for the three Dalitz regions, after full selection. Both magnet polarities and data-taking years are added. The $D_s^{\mp}$ signal yield is indicated in yellow, while the $D^{\mp}$ yield is indicated in red.

5

Sample	Dalitz region		
	$\phi\pi$	K^*K	NR
Yields			
2011 Magnet up	113 442	52 650	35 417
2011 Magnet down	156 104	72 436	48 787
2012 Magnet up	325 005	148 359	101 288
2012 Magnet down	304 151	139 139	94 943
$\boldsymbol{A_{\text{meas}}}$ [%]			
2011 Magnet up	1.54 ± 0.32	1.31 ± 0.49	1.24 ± 0.65
2011 Magnet down	-1.97 ± 0.27	-1.13 ± 0.41	-1.56 ± 0.55
2012 Magnet up	0.28 ± 0.19	0.41 ± 0.29	1.16 ± 0.38
2012 Magnet down	0.01 ± 0.19	-0.12 ± 0.30	0.01 ± 0.40

Table 5.3: Yields and measured asymmetries in % including their statistical uncertainties, as obtained from fits to the invariant mass of D_s^- and D_s^+ candidates, separately for each Dalitz region, magnet polarity and data-taking year.

sum over Dalitz regions is followed by an arithmetic average of the two magnet polarities, and a weighted average of the two data-taking years, resulting in

$$A_{\text{meas}} = (0.11 \pm 0.09)\% \,. \tag{5.2.3}$$

A possible mismodelling of the mass peak might be a source of bias in the measured asymmetry. This is checked by performing a study using a sum of a double-sided Crystal Ball function (Eq. 3.4.2) and a Gaussian, instead of the Hypatia function for the signal shape, which is found to describe the data equally well. In order to quantify the difference in the fitted yields with both shapes, without double-counting the statistical error, events are generated using the alternative shape for the signal, and the nominal shape for the backgrounds. When the nominal fit is applied to these generated events, only a small bias on A_{meas} of 0.02% is observed in the *NR* region. This bias is most likely due to a correlation with the asymmetric combinatorial background. In addition, the fixed tail parameters of the signal shape are varied within their uncertainty. The resulting deviations from the nominal values for A_{meas} are negligible for the $\phi\pi$ region, and between 0.00% and 0.02% for the K^*K and *NR* regions. In the combination of all data, a total systematic error of 0.018% on the measured asymmetry is assigned to all these effects.

5.3 Simulation and peaking backgrounds

In order to study the signal and background composition, simulated events are generated. They are used to determine the relative contributions of the various backgrounds that are included in the measured asymmetry, which enter explicitly in the determination of a^s_{sl} (Eq. 5.1.1). The composition of the simulated samples is discussed below, after which the contributions of the backgrounds to the measurement of a^s_{sl} are discussed.

5.3.1 Signal simulation

The signal sample consists of 20 million B^0_s mesons that are forced to decay to a $D^-_s\mu^+\nu_\mu X$ final state, including resonances. The D^-_s is forced to decay to $K^-K^+\pi^-$ using a phase-space model that includes the known resonances. Absolute branching ratios are obtained from Ref. [94], resulting in a contribution of 23% to the total sample for $B^0_s \to D^-_s\mu^+\nu_\mu$ decays. Contributions from B^0_s decays to higher charmed resonances, for which $X = \gamma, \pi^0, \pi^+\pi^-$, contribute 72% to the sample, and are dominated by $B^0_s \to D^{*-}_s\mu^+\nu_\mu$ decays. Decays involving a B^0_s decaying semileptonically to a τ^+, which in turn decays as $\tau^+ \to \mu^+\overline{\nu}_\tau\nu_\mu$, contribute about 5%.

5.3.2 Contributions from peaking backgrounds

The contributions of various backgrounds that peak in the D^-_s mass, will dilute the sensitivity of the measured asymmetry to a^s_{sl}. These contributions are estimated using a cocktail of simulated $D^-_s \to K^+K^-\pi^-$ decays. This includes decays from Λ^0_b, B^+,

$\overline{B}^0$ and B_s^0. After full selection, 85% of the candidates originate from the signal decay $B_s^0 \to D_s^- \mu^+ \nu_\mu X$. About 6% of the candidates originate from combinatorial D_s^- decays. About 1.5% originates from misidentified $B_s^0 \to D_s^- \mu^+{}_{\pi^+,K^+} X$ decays, or real $B_s^0 \to D_s^-$ transitions where the muon originates from a semileptonic decay of another b hadron. These decays behave similar to the signal, in the sense that they are sensitive to *CP* violation in the B_s^0 mixing process.

The dominant source of peaking backgrounds contains b-hadron decays into two charmed mesons, in which a D_s^+ is produced from the virtual W^+ and the other charmed hadron decays semileptonically. Combined, these doubly-charmed backgrounds contribute about 10% to the selected candidates. Finally, there is a contribution of about a percent from $B^+ \to D_s^- \mu^+ K^- \nu_\mu X$ and $B^0 \to D_s^- \mu^+ \overline{K}^0 \nu_\mu X$ decays.

The dominant backgrounds described above contain additional particles with respect to the $B_s^0 \to D_s^- \mu^+ \nu_\mu X$ signal mode. Their contribution is already reduced by the momentum cut on the muon and the cut on the corrected B_s^0 mass as shown in Fig. 5.6. Dedicated simulated samples containing at least 5 million events are generated for each of these modes to determine the selection efficiencies.

The production rates of the different b hadrons with respect to the B_s^0 meson are quantified by the b-hadron fractions [105, 110],

$$\begin{aligned} f_u/f_s = f_d/f_s &= 3.86 \pm 0.22 \\ f_{\Lambda_b^0}/f_s &= 2.34 \pm 0.31, \end{aligned} \tag{5.3.1}$$

where f_u is the production rate of B^+ mesons, f_s is the production rate of B_s^0 mesons, f_d is the production rate of B^0 mesons and $f_{\Lambda_b^0}$ is that of Λ_b^0 mesons. In the determination of $f_{\Lambda_b^0}/f_s$, the p_{T}-dependent production rate in Ref. [105] is taken into account. The branching ratios of these modes are taken from Ref. [94]. The relative selection efficiencies, production rates and branching ratios are summarized in Table 5.4. Besides diluting the measured asymmetry, these backgrounds can have a charge asymmetry, which would bias the measured value of a_{sl}^s. The asymmetry in these backgrounds is determined below.

5.3.3 Asymmetries in the background modes

The B^+ production asymmetry was determined in Sec. 4.4.5 to be $A_{P,B^+} = (-0.6 \pm 0.6)\%$, with the largest uncertainty originating from the measured *CP* asymmetry of $A_{CP}(B^+ \to J/\psi K^+) = (0.3 \pm 0.6)\%$. The B^0 background asymmetry originates from both the production asymmetry and a_{sl}^d. Both are taken from the a_{sl}^d analysis described in Chapter 4. The time-integrated asymmetries are diluted due to the B^0 oscillations, that go as $\cos(\Delta m_d t)$ for A_{P,B^0}, and as $1 - \cos(\Delta m_d t)$ for $a_{\mathrm{sl}}^d/2$ (see Eq. 1.2.42). Using the values of the lifetime and Δm_d from Ref. [94] and the decay-time acceptance from Eq. 4.4.11 this results in a dilution factor of 0.36 on A_{P,B^0} and 0.64 on $a_{\mathrm{sl}}^d/2$. Adding both effects, and averaging over the statistically compatible centre-of-mass energies, the result is

$$A_{\mathrm{bkg},B^0}^{\mathrm{eff}} = (-0.18 \pm 0.13)\%. \tag{5.3.2}$$

Table 5.4: Branching fractions ($\mathcal{B}$), efficiency ratios ($\varepsilon_{\rm sig}/\varepsilon_{\rm bkg}$), background-over-signal ratio ($f_{\rm bkg}/f_{\rm sig}$) and effective asymmetries for the different background sources. The branching fractions are obtained from Ref. [94]. The signal branching fraction is $\mathcal{B} = (7.9 \pm 2.4)\%$. The b-hadron fractions from the pp collision are $f_u/f_s = f_d/f_s = (3.86 \pm 0.22)$ [110] and $f_{\Lambda_b^0}/f_s = (2.34 \pm 0.31)$ [105].

Mode	$\mathcal{B}$ [%]	$\mathcal{B}(c \to \mu)$ [%]	$\varepsilon_{\rm sig}/\varepsilon_{\rm bkg}$	$f_{\rm bkg}/f_{\rm sig}$ [%]	$A_{\rm bkg}$ [%]
$B^+ \to D^{(*)0} D_s^{(*)+} X$	7.9 ± 1.4	6.5 ± 0.1	4.34	5.8 ± 1.1	-0.6 ± 0.6
$B^0 \to D^0 D_s^{(*)+} X$	5.7 ± 1.2	6.5 ± 0.1	4.08	4.4 ± 1.0	-0.18 ± 0.13
$B^0 \to D^- D_s^{(*)+} X$	4.6 ± 1.2	16.1 ± 0.3	6.41	5.6 ± 1.5	-0.18 ± 0.13
$B_s^0 \to D_s^{(*)-} D_s^{(*)+}$	4.5 ± 1.4	8.1 ± 0.4	3.68	1.0 ± 0.3	–
$\Lambda_b^0 \to \Lambda_c^+ D_s^{(*)+} X$	$10.3^{+2.1}_{-1.8}$	4.5 ± 1.7	4.51	3.0 ± 1.4	$+0.5 \pm 0.8$
$B^- \to D_s^+ K^- \mu^- \nu X$	0.061 ± 0.010	–	2.43	1.3 ± 0.2	0.6 ± 0.6
$\overline{B}^0 \to D_s^+ K_S^0 \mu^- \nu X$	0.061 ± 0.010	–	2.89	1.1 ± 0.2	0.18 ± 0.13

The asymmetry of the $B_s^0 \to D_s^- D_s^+$ background has a negligible contribution from a production asymmetry in the time-integrated analysis, due to the fast oscillation frequency Δm_s. Furthermore, due to charge-symmetric final state, the total contribution from CP violation (or A_P) in this mode is negligible, and this background only dilutes the raw asymmetry.

The production asymmetry of Λ_b^0 baryons is estimated using the combined CP and production asymmetry of $A_{\rm meas}(\Lambda_b^0 \to J/\psi p^+ K^-) = (-0.1 \pm 0.7)\%$ [111]. Correcting for the CP asymmetry in this decay, which is estimated to be $A_{CP}(\Lambda_b^0 \to J/\psi p^+ K^-) = (-0.6 \pm 0.3)\%$ [107, 112], this becomes

$$A_{{\rm P},\Lambda_b^0} = (+0.5 \pm 0.8)\%. \tag{5.3.3}$$

A paper containing new LHCb measurements of the production asymmetry of B^0, B_s^0, B^+ and $\overline{\Lambda}_b^0$ mesons, using alternative decay channels, is currently undergoing review [113]. They are statistically compatible with the values used in this section, but the uncertainties are larger compared to those determined in this section. In addition, a measurement of the $\overline{\Lambda}_b^0$ production asymmetry using semileptonic decays in LHCb is currently ongoing. The expected uncertainty on these measurements is about 0.3%.

5.3.4 Effect on $a_{\rm sl}^s$

The total fraction of each background is calculated using the relative production rates, branching ratios, and relative selection efficiencies as obtained from the dedicated simulated samples. They are summarized in Table 5.4, and add up to a dilution of the raw asymmetry of

$$f_{\rm bkg} \equiv \sum_i f_{\rm bkg}^i = (18.4 \pm 6.0)\%. \tag{5.3.4}$$

The asymmetries in the background modes are shown in the last column of Table 5.4, and add up to a bias on $a_{\rm sl}^s$ of

$$f_{\rm bkg}A_{\rm bkg} \equiv \sum_i f_{\rm bkg}^i A_{\rm bkg}^i = (-0.023 \pm 0.031)\%. \tag{5.3.5}$$

5.4 Detection asymmetries

This section is dedicated to the detection asymmetries, using the methods from Chapter 3. Four contributions are discerned: the $\mu^+\pi^-$ asymmetry, the K^+K^- asymmetry, the trigger asymmetry and the asymmetry due to PID criteria.

5.4.1 The $\mu^+\pi^-$ asymmetry

In contrast to the $a_{\rm sl}^d$ analysis, both the J/ψ tag-and-probe method and the D^* partial-and-full methods from Sec. 3.1 are employed. The asymmetry arising from the different kinematic distributions of the μ^+ and π^- is covered by the combination of these two methods. This means that no weights are applied to match the π^- kinematic distributions to those of the μ^+. Again, any tracking asymmetry is expected to disappear when both distributions are equal. The $\mu^+\pi^-$ asymmetry is calculated from either method by using the difference in the kinematic distributions of the μ^+ and π^-, as outlined in Sec. 3.1. The overlap of the signal muon and pion distributions is shown in Fig. 5.8, and slightly depends on the Dalitz region.

The results of both methods are compared in Table 5.5, where the simulation studies described in Sec. 3.1.3 are used to assign an additional systematic error due to different material cross-sections between muons and pions, and a different amount of material that is traversed by particles of either charge, depending on the magnet polarity. The J/ψ tag-and-probe method is corrected for the limited acceptance of the muons. Both methods are in good agreement.

The total $\mu^+\pi^-$ asymmetry used to correct $A_{\rm meas}$ is calculated by taking the weighted average of both methods, using only the statistical error when calculating the weights. In the magnet-average result, the systematic errors and correction to the J/ψ method, resulting from the simulation studies, are much smaller. Hence, no correction is applied and only a systematic error is assigned, which is 0.02% for all Dalitz regions, magnet polarities and data-taking years combined. The resulting values for the $\mu^+\pi^-$ tracking asymmetry are shown together with all other asymmetries at the end of this section in Table 5.10.

5.4.2 The K^+K^- asymmetry

The kaon detection asymmetry is of the order of a percent due to a difference in cross-sections of incident K^+ and K^- onto the detector material, as discussed in Sec. 3.2. However, when constructing an asymmetry of K^+K^- pairs, the asymmetry is expected

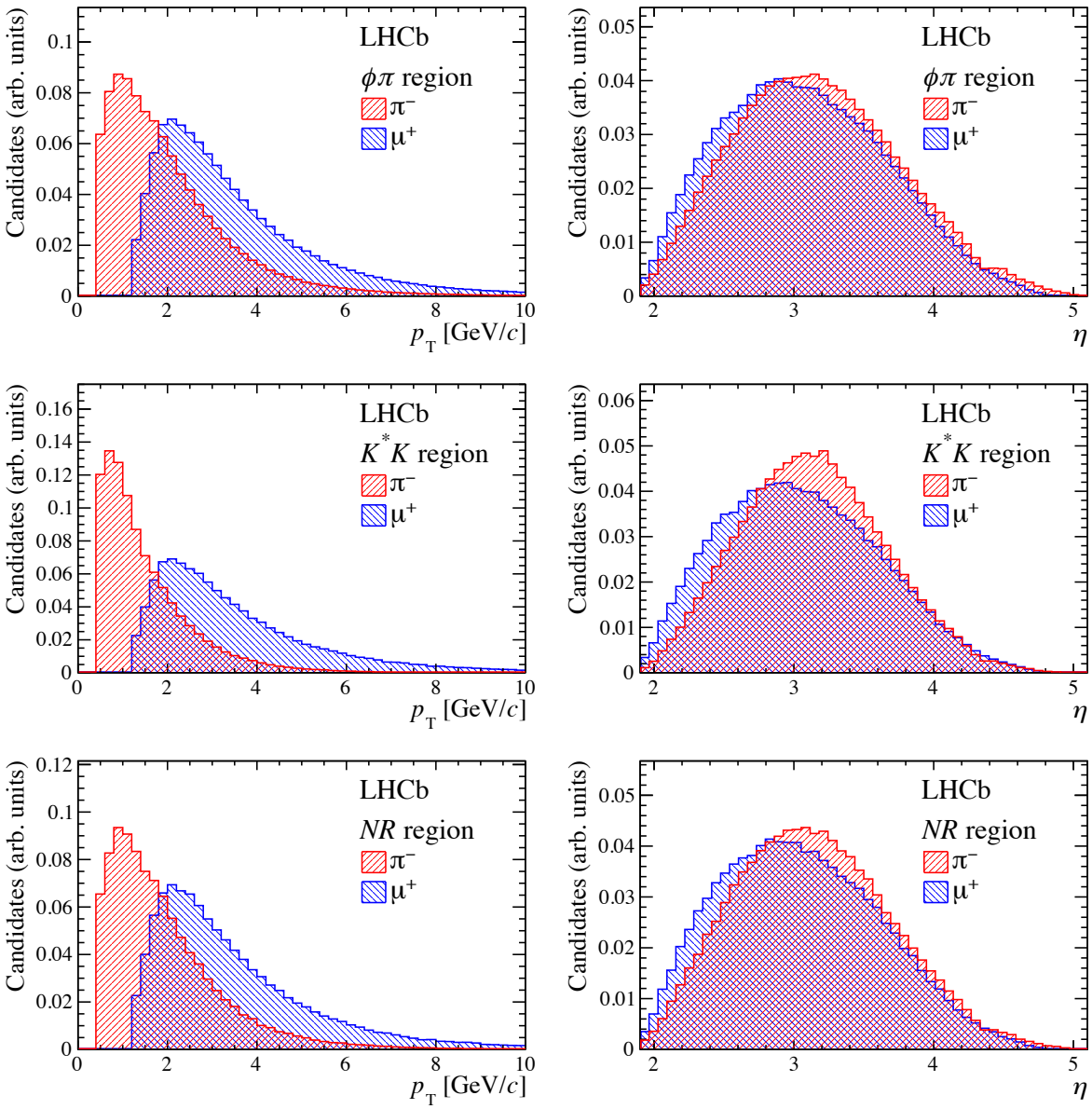

Figure 5.8: The background-subtracted p_T and η distributions of the final-state pion and muon. For these histograms all data including both years and both magnet polarities are combined.

to cancel if there is perfect kinematic overlap between the kaons. The overlap of the kinematic distributions of the kaon with the same sign (SS) and opposite sign (OS) as the D_s^- are shown in Fig. 5.9, and is in general very good. In the $\phi\pi$ region the kinematic distributions are nearly identical, as they come from the same resonance ($\phi(1020)$) and due to the small available phase space in this decay. In the other two regions the difference between the distributions is somewhat larger.

The K^+K^- asymmetry is calculated using the method from Sec. 3.2.1, and the resulting values are shown in Table 5.6. In the $\phi\pi$ region the asymmetry is small, due to the good kinematic overlap. In the other regions it is found to be somewhat larger. The total

Table 5.5: Asymmetry comparison of J/ψ and D^* method, split by magnet polarity, in percent. The first error is statistical, the second systematic. Simulation studies are performed to assign additional systematic errors, and to correct the J/ψ method in order to make a comparison in terms of the absolute difference and the difference in number of standard deviations $N(\sigma)$.

	D^* method	J/ψ method	Difference	$N(\sigma)$
2011, Magnet up				
$\phi\pi$	$0.26 \pm 0.26 \pm 0.08$	$0.27 \pm 0.15 \pm 0.14$	-0.01 ± 0.34	-0.03
K^*K	$0.46 \pm 0.46 \pm 0.10$	$0.25 \pm 0.16 \pm 0.13$	0.21 ± 0.51	0.41
NR	$0.30 \pm 0.29 \pm 0.09$	$0.27 \pm 0.16 \pm 0.13$	0.03 ± 0.37	0.08
2011, Magnet down				
$\phi\pi$	$-0.19 \pm 0.20 \pm 0.09$	$-0.28 \pm 0.13 \pm 0.17$	0.09 ± 0.31	0.29
K^*K	$-0.34 \pm 0.34 \pm 0.11$	$-0.25 \pm 0.14 \pm 0.15$	-0.09 ± 0.41	-0.22
NR	$-0.23 \pm 0.24 \pm 0.09$	$-0.21 \pm 0.14 \pm 0.13$	-0.02 ± 0.32	-0.06
2012, Magnet up				
$\phi\pi$	$0.26 \pm 0.14 \pm 0.09$	$0.15 \pm 0.10 \pm 0.14$	0.11 ± 0.24	0.46
K^*K	$0.46 \pm 0.23 \pm 0.12$	$0.14 \pm 0.11 \pm 0.14$	0.32 ± 0.31	1.03
NR	$0.31 \pm 0.16 \pm 0.10$	$0.12 \pm 0.11 \pm 0.13$	0.19 ± 0.25	0.76
2012, Magnet down				
$\phi\pi$	$-0.27 \pm 0.13 \pm 0.10$	$-0.24 \pm 0.10 \pm 0.15$	-0.03 ± 0.24	-0.13
K^*K	$-0.46 \pm 0.22 \pm 0.13$	$-0.24 \pm 0.10 \pm 0.18$	-0.22 ± 0.33	-0.67
NR	$-0.32 \pm 0.16 \pm 0.10$	$-0.22 \pm 0.10 \pm 0.15$	-0.10 ± 0.26	-0.38

systematic error resulting from the studies described in Sec. 3.2.1 is 0.034% when taking the average over the Dalitz regions, magnet polarities and data-taking years.

Table 5.6: K^+K^- asymmetry for the three Dalitz regions, obtained by weighing the calibration samples to the signal kaon kinematic distributions .

Sample	A_{KK} per Dalitz region [%]		
	$\phi\pi$	K^*K	NR
2011 Magnet up	0.010 ± 0.002	-0.043 ± 0.008	-0.059 ± 0.012
2011 Magnet down	0.010 ± 0.002	-0.003 ± 0.009	-0.031 ± 0.012
2012 Magnet up	0.015 ± 0.002	-0.057 ± 0.009	-0.086 ± 0.012
2012 Magnet down	0.001 ± 0.002	0.004 ± 0.009	-0.005 ± 0.012

5.4.3 PID asymmetry

In contrast to the $a_{\rm sl}^d$ analysis, the kaon PID criteria using `DLL` variables are softer in the selection of data (see Table 5.2) than they are in the determination of the K^+K^-

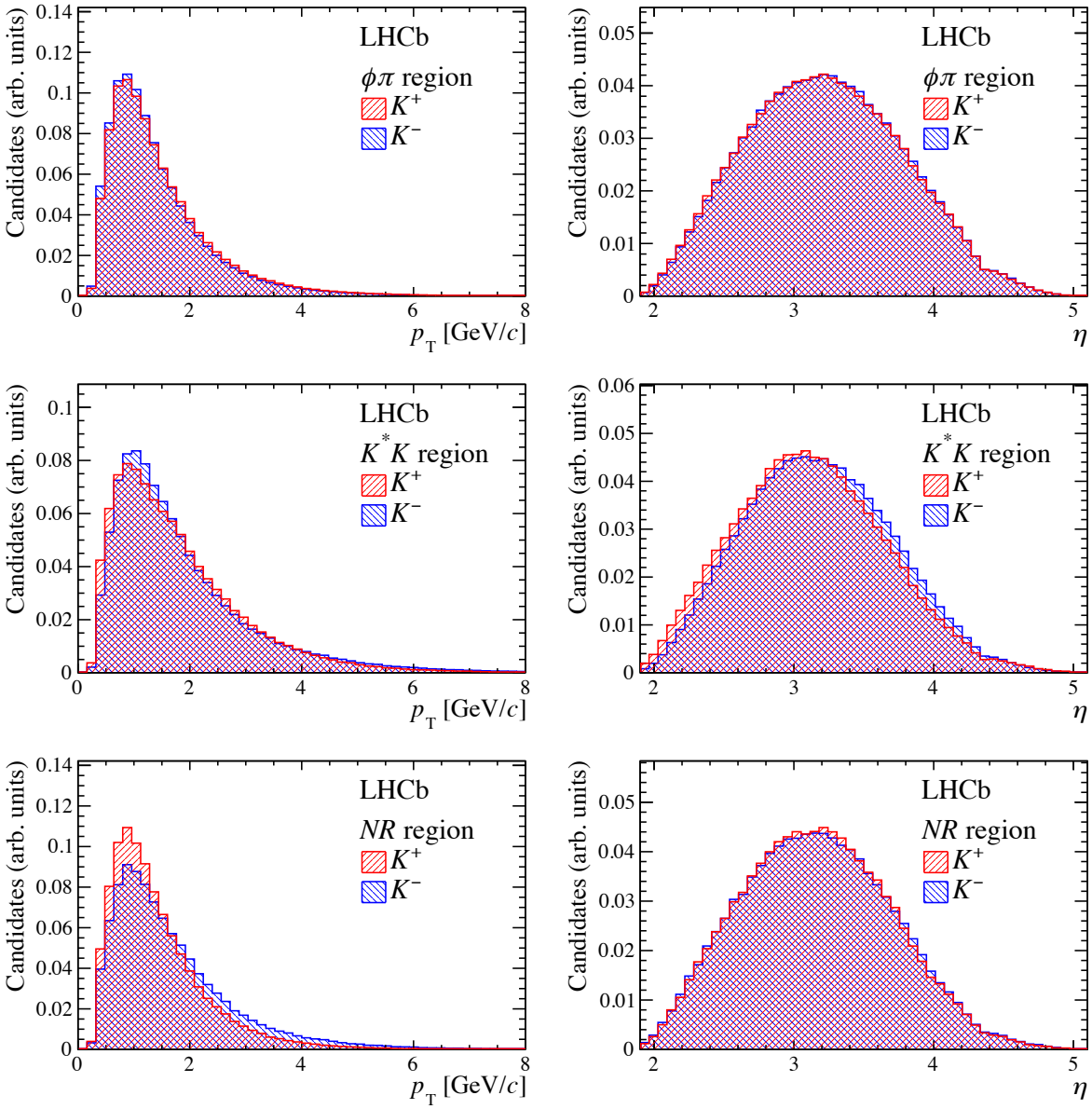

Figure 5.9: The background-subtracted p_T and η distributions of the final-state kaons. For these histograms all data including both years and both magnet polarities are combined.

asymmetry (Sec. 5.4.2). Therefore, the asymmetry due to PID in the calibration samples that are used to determine the K^+K^- asymmetry, are corrected for. These corrections are determined using the method of Sec. 3.3, based on $D^{*-} \to D^0(\to K^-\pi^+)\pi^-$ decays. The size of these corrections to A_{KK} is negligible in the $\phi\pi$ region, and are small (ranging from -0.03% up to 0.05%) in the other regions, due to the two oppositely-charged kaons. These corrections are already included in Table 5.6.

The PID asymmetry of the signal selection due to the PID criteria is determined separately. In addition to the cut on the kaon log-likelihood variable `DLL`, a cut is made on the neural-net variable `ProbNN` of the same-sign kaon. On the pion, a loose `DLL` cut is made

for the K^*K and NR regions. This is not done for the $\phi\pi$ region.[2] Besides these global PID requirements, the vetoes of the identifiable backgrounds in Sec. 5.2 require strong PID requirements for specific mass regions in the data. The asymmetries of these vetoes are determined by using the same method of Sec. 3.3, and only sampling the kinematic distributions of the data that lie within the specific mass region that is relevant to that veto. The resulting asymmetries are large, but the overall effect is small since they only apply to a small part of the data.

The total PID asymmetry is determined by summing the individual PID asymmetries of the selections on the various particles in the final state. The large correlations between the different asymmetries, when obtained from the same calibration sample, are taken into account. In the sum, the asymmetries of the vetoes are weighed by the amount of data they apply to. The dominant contribution originates from the global PID cuts on the kaons and reaches up to 6%, although it largely cancels due to the contribution of the other kaon in the final state. The total PID asymmetries are shown in Table 5.7, including the systematic errors described in Sec. 3.3.

Table 5.7: Total PID asymmetry, split up by year and Dalitz region, including the statistical error.

Sample	A_{PID} per Dalitz region [%]		
	$\phi\pi$	K^*K	NR
2011 Magnet up	0.01 ± 0.05	0.08 ± 0.07	0.06 ± 0.08
2011 Magnet down	-0.01 ± 0.04	-0.11 ± 0.06	-0.07 ± 0.07
2012 Magnet up	0.01 ± 0.03	0.04 ± 0.04	0.01 ± 0.05
2012 Magnet down	-0.01 ± 0.03	-0.14 ± 0.04	-0.07 ± 0.05

5.4.4 The trigger and muon PID asymmetry

The asymmetry of the muon hardware-level trigger and PID is determined using a tag-and-probe method using $B \to J/\psi X$ decays (see Sec. 3.4). The resulting asymmetries are shown in Table 5.8. Unlike the a_{sl}^d analysis, no look-up-table has been used to correct the bias due to the p_{T} estimate in the hardware-level trigger. Hence, the trigger asymmetries in the 2011 data for this analysis are larger than those for the a_{sl}^d analysis. After correcting the raw asymmetry for the trigger asymmetry, this choice should not make a difference in the obtained value for a_{sl}^s, for each magnet polarity and data-taking year. Also, the magnet-average asymmetries are compatible with zero, ensuring that the averaged result for a_{sl}^s is unaffected by this choice.

In contrast to the a_{sl}^d analysis, the asymmetry from the software-level trigger is treated separately, as was described in Sec. 3.4.1. This is because a combination of two software triggers is used: one using the muon (`Hlt1TrackMuon`), and another triggering on any of

[2] A description of the `DLL` and `ProbNN` variables is made in Sec. 2.3.4.

Sample	A_μ per Dalitz region [%]		
	$\phi\pi$	K^*K	NR
2011 Magnet up	1.10 ± 0.06	1.02 ± 0.06	1.01 ± 0.06
2011 Magnet down	-1.17 ± 0.07	-1.09 ± 0.05	-1.13 ± 0.05
2012 Magnet up	0.06 ± 0.04	0.09 ± 0.04	0.03 ± 0.04
2012 Magnet down	-0.12 ± 0.04	-0.13 ± 0.04	-0.18 ± 0.04

Table 5.8: Muon trigger and PID asymmetries, without the software-level trigger requirement, including the statistical errors only. In 2011 no look-up-table was applied to correct for the hardware-level p_{T} effect.

the four final-state tracks (`Hlt1TrackAllL0`). The resulting asymmetries are shown in Table 5.9, which also contains the corresponding systematic uncertainties. In addition, the second-level software trigger adds a systematic error of 0.020%, the same as in the a^d_{sl} analysis.

Table 5.9: The combined software-level trigger asymmetries in the a^s_{sl} sample, for each Dalitz region, split up by magnet polarity and data-taking year. The uncertainties are statistical only.

Sample	A_{Hlt} per Dalitz region [%]		
	$\phi\pi$	K^*K	NR
2011 magnet up	-0.04 ± 0.02	-0.05 ± 0.02	-0.04 ± 0.01
2011 magnet down	0.12 ± 0.03	0.14 ± 0.03	0.11 ± 0.02
2012 magnet up	-0.04 ± 0.02	-0.05 ± 0.02	-0.04 ± 0.01
2012 magnet down	0.10 ± 0.01	0.11 ± 0.01	0.09 ± 0.01

5.4.5 Total detection asymmetry

The combinations of the detection asymmetries for both magnet polarities and data-taking years are shown in Table 5.10. The systematic errors on the magnet-average results are significantly smaller than those for the individual magnet polarities, as discussed in the above sections.

5.5 Results

The measured asymmetries of Table 5.3 are corrected for the detection- and background asymmetry, as per Eq. 5.1.1. The dilution factor due to the background acts as a multiplicative factor to both the central value and the errors. This factor is calculated

Table 5.10: Detection asymmetries in % for both magnet polarities and data-taking years combined, for each Dalitz region, including statistical error. The last column is the average over the three Dalitz regions. For $A_{\mu\pi}$ the average of the D^* and J/ψ methods is used. A_μ is the muon hardware trigger and PID asymmetry, while A_{Hlt} is the combined software-level trigger asymmetry. The detection asymmetries are uncorrelated between each other, and assumed to be fully correlated between Dalitz regions. In the last column, the second error is the combined systematic error.

A_{det}	$\phi\pi$	K^*K	NR	Average
$A_{\mu\pi}$	-0.01 ± 0.05	0.00 ± 0.06	0.00 ± 0.05	$-0.01 \pm 0.05 \pm 0.04$
A_{KK}	0.01 ± 0.00	-0.03 ± 0.00	-0.05 ± 0.01	$-0.01 \pm 0.00 \pm 0.03$
A_{PID}	-0.00 ± 0.02	0.04 ± 0.03	0.02 ± 0.03	$0.01 \pm 0.02 \pm 0.02$
A_μ	-0.03 ± 0.02	-0.03 ± 0.02	-0.07 ± 0.02	$-0.03 \pm 0.02 \pm 0.02$
A_{Hlt}	0.00 ± 0.01	0.01 ± 0.01	0.00 ± 0.01	$0.00 \pm 0.01 \pm 0.01$
Total	-0.03 ± 0.06	-0.01 ± 0.07	-0.09 ± 0.06	$-0.03 \pm 0.06 \pm 0.06$

from the value of f_{bkg} in Sec. 5.3, and is

$$\frac{2}{1 - f_{\text{bkg}}} = 2.45 \pm 0.18 \tag{5.5.1}$$

Using the detection asymmetries from Table 5.10 and the background fraction and asymmetry of Sec. 5.3.4, the resulting values of a^s_{sl} with their statistical error are shown in Table 5.11. In contrast to the a^d_{sl} analysis, the statistical errors represent the quadratic sum of the statistical errors on both A_{meas} and on the detection asymmetries A_{det}. The individual contributions to the total statistical errors are shown in Table 5.11.

Figure 5.10 is a graphical representation of the values of a^s_{sl}, including each of the twelve data sets. They are found to be compatible within statistical fluctuations. Since the non-peaking backgrounds and detection asymmetries can vary significantly between Dalitz regions, an additional consistency check is made. Using only the uncorrelated statistical errors, the difference of the combined value of a^s_{sl} in the $\phi\pi$ region, $(0.16 \pm 0.25)\%$, with the value in the combined K^*K and NR regions, $(0.76 \pm 0.39\%)$, is 1.5 standard deviations. A further consistency check between Dalitz regions is done using prompt $D_s^- \to K^+K^-\pi^-$ decays, of which LHCb has recorded almost a factor 10 more events in run 1 compared to $B_s^0 \to D_s^-(\to K^+K^-\pi^-)\mu^+\nu_\mu$ decays. This mode can be used to measure the D_s^- production asymmetry, which should be independent of the D_s^- Dalitz region. The D_s^- production asymmetry is indeed found to be consistent [114].

The combination of the various Dalitz regions, magnet polarities and data-taking years, including statistical and systematic errors, is summarized in Table 5.12. In order to take into account the error on the background dilution factor, the systematic error due to $A_{\text{meas}} + A_{\text{det}}$ is multiplied by the sum of the dilution factor plus its error, in order to obtain the total systematic error on a^s_{sl}. The final result is

$$a^s_{\text{sl}} = (0.39 \pm 0.26 \pm 0.20)\%, \tag{5.5.2}$$

Table 5.11: Values of $a^s_{\rm sl}$ in % for each Dalitz region, magnet polarity and data-taking year, as obtained using Eq. 5.1.1. The values shown are statistical only. These values are graphically represented by Fig. 5.10.

	2011, Up	2011, Down	2012, Up	2012, Down	Total
$\phi\pi$	0.95 ± 0.87	−2.07 ± 0.74	0.55 ± 0.52	0.37 ± 0.52	0.16 ± 0.31
K^*K	0.52 ± 1.27	0.10 ± 1.08	0.91 ± 0.76	0.26 ± 0.77	0.50 ± 0.45
NR	0.43 ± 1.65	−0.82 ± 1.40	3.02 ± 0.97	0.62 ± 1.01	1.22 ± 0.59
Average	0.77 ± 0.72	-1.36 ± 0.62	0.98 ± 0.44	0.38 ± 0.44	0.39 ± 0.26

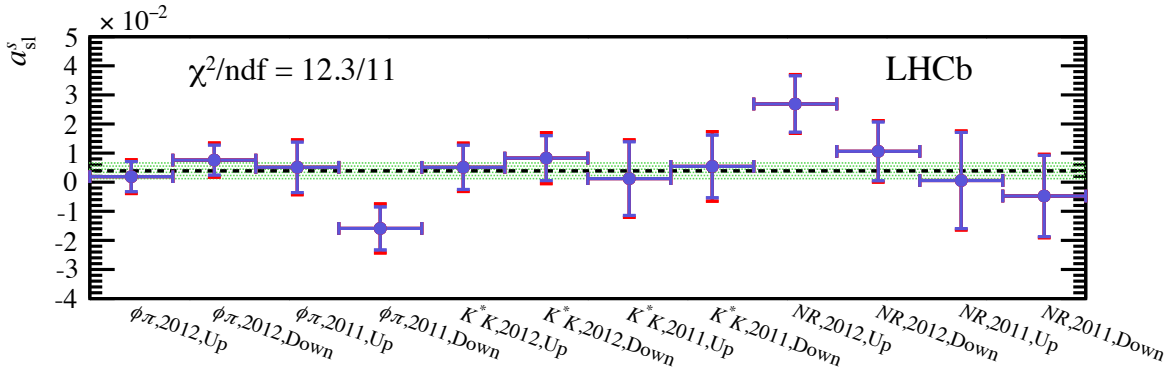

Figure 5.10: The values of $a^s_{\rm sl}$ for all Dalitz regions, magnet polarities and data-taking years separately. The blue error bar indicates the statistical error, while the red error bar in addition takes into account magnet-dependent systematic effects. The black dashed line indicates the value of the nominal combination, the error of which is displayed by the green-dotted region.

where the first error is the combination of statistical errors on the measured asymmetry and detection asymmetries, and the second error is the total systematic error. A discussion of this result is done in Chapter 6.

Table 5.12: Overview of contributions in the determination of $a^s_{\rm sl}$, averaged over Dalitz regions, magnet polarities and data-taking periods, with their statistical and systematic uncertainties. All numbers are in percent. The central value of $a^s_{\rm sl}$ is calculated according to Eq. 5.1.1. The uncertainties are added in quadrature and multiplied by $2/(1-f_{\rm bkg})$, which is the same for all twelve subsamples, to obtain the uncertainties on $a^s_{\rm sl}$.

Source	Value	Stat. uncert.	Syst. uncert.	
$A_{\rm meas}$	0.11	0.09	0.02	
$-A_{KK}$	0.01	0.00	0.03	
$-A_{\mu\pi}$	0.01	0.05	0.04	
$-A_{\rm PID}$	−0.01	0.02	0.03	
$-A_{\mu}$	0.03	0.02	0.02	
$-A_{\rm Hlt}$	0.00	0.01	0.02	
$-f_{\rm bkg}\ A_{\rm bkg}$	0.02	−	0.03	+
$(1-f_{\rm bkg})a^s_{\rm sl}/2$	0.16	0.11	0.08	
$2/(1-f_{\rm bkg})$	2.45	−	0.18	×
$a^s_{\rm sl}$	0.39	0.26	0.20	